

## Convection and Dynamo in Newly-born Neutron Stars

YOUHEI MASADA,<sup>1</sup> TOMOYA TAKIWAKI,<sup>2</sup> AND KEI KOTAKE<sup>3</sup>

<sup>1</sup>*Department of Science Education, Aichi University of Education, Kariya 448-8542, Japan*

<sup>2</sup>*Division of Science, National Astronomical Observatory of Japan, Tokyo 181-8588, Japan*

<sup>3</sup>*Faculty of Science, Department of Applied Physics & Research Institute of Stellar Explosive Phenomena, Fukuoka University, Fukuoka 814-0180, Japan*

(Received April 28, 2022)

Submitted to ApJ

### ABSTRACT

To study properties of magneto-hydrodynamic (MHD) convection and resultant dynamo activities in proto-neutron stars (PNSs), we construct a “PNS in a box” simulation model with solving compressible MHD equation coupled with a nuclear equation of state (EOS) and a simplified leptonic transport. As a demonstration, we apply it to two types of PNS models with different internal structures: fully-convective model and spherical-shell convection model. By varying the spin rate of models, the rotational dependence of convection and dynamo that operate inside the PNS is investigated. We find that, as a consequence of turbulent transport by rotating stratified convections, large-scale structures of flow and thermodynamic fields are developed in all models. Depending on the spin rate and the convection zone depth, various profiles of the large-scale structures are obtained, which can be physically understood as steady-state solutions to the “mean-field” equation of motion. Additionally to those hydrodynamic structures, the large-scale magnetic component with  $\mathcal{O}(10^{15})$  G is also spontaneously organized in disordered tangled magnetic field in all models. The higher the spin rate, the stronger the large-scale magnetic component is built up. Intriguingly, as an overall trend, the fully-convective models have a stronger large-scale magnetic component than that in the spherical-shell convection models. The deeper the convection zone extends, the larger the size of the convection eddies becomes. As a result, the rotationally-constrained convection seems to be more easily achieved in the fully-convective model, resulting in the higher efficiency of the large-scale dynamo there. To gain a better understanding of the origin of the diversity of NS’s magnetic field, we need to study the PNS dynamo in a wider parameter range.

*Keywords:* convection — dynamo — magneto-hydrodynamics (MHD) — stars: magnetic field — stars: neutron

### 1. INTRODUCTION

Neutron stars (NSs) have the most extreme magnetic field in the universe, typically trillion, up to quadrillion times more powerful than Earth’s. Although, we know, they are formed as an aftermath of massive stellar core-collapse, the origin of the magnetic field is still an outstanding issue in astrophysics. Mainly, two possible ori-

gins have been proposed: fossil field and dynamo field hypotheses (e.g., Spruit 2008; Ferrario et al. 2015). While the former regards it as an inheritance from NS’s main sequence progenitor (e.g., Ruderman 1972), the later presumes that it would be generated by some dynamo processes in newly-born NSs, also known as proto-neutron stars (PNSs) (e.g., Ruderman & Sutherland 1973; Thompson & Duncan 1993, hereafter TD93).

One important physical process, which should be examined further in either scenarios, is the role of PNS convection. Even if the strong fossil field exists before the collapse, it should be subjected to vigorous convec-

**Table 1.** Summary of the simulation runs. The models with prefixes mf & ms correspond to the models with the full-sphere CZ and spherical-shell CZ. The mean quantities  $v_{\text{mean}}$ ,  $Ro_{\text{mean}}$ ,  $\langle \epsilon_{\text{M}} \rangle$  ( $\langle \epsilon_{\text{K}} \rangle$ ) are evaluated at the saturated state, where  $v_{\text{mean}} \equiv \langle (v_r - \langle v_r \rangle_{\phi})^2 \rangle_V^{1/2}$  and  $Ro_{\text{mean}} \equiv v_{\text{mean}} / (2\Omega_0 w_{\text{cz}})$  with the width of the CZ,  $w_{\text{cz}}$ , for each model, *model* mf ( $w_{\text{cz}} = 15\text{km}$ ) or *model* ms ( $w_{\text{cz}} = 7\text{km}$ ).

	$\Omega_0$	$R_d$ [km]	$v_{\text{mean}}$ [km/s]	$Ro_{\text{mean}}$	$\langle \epsilon_{\text{K}} \rangle$ [erg/cm <sup>3</sup> ]	$\langle \epsilon_{\text{M}} \rangle$ [erg/cm <sup>3</sup> ]	$\epsilon_{\text{Mm}}^{l=1-3}$ [erg/cm <sup>3</sup> ]
mf12p	$12\pi$	17.5	$9.18 \times 10^2$	0.81	$3.73 \times 10^{30}$	$9.59 \times 10^{29}$	$2.51 \times 10^{25}$
mf60p	$60\pi$	17.5	$7.47 \times 10^2$	0.13	$2.99 \times 10^{30}$	$8.90 \times 10^{29}$	$5.83 \times 10^{26}$
mf120p	$120\pi$	17.5	$6.66 \times 10^2$	0.06	$2.99 \times 10^{30}$	$8.14 \times 10^{29}$	$4.14 \times 10^{27}$
ms100p	$100\pi$	17.0	$2.19 \times 10^3$	0.50	$6.75 \times 10^{30}$	$1.46 \times 10^{30}$	$3.75 \times 10^{25}$
ms300p	$300\pi$	17.0	$2.01 \times 10^3$	0.15	$5.75 \times 10^{30}$	$1.30 \times 10^{30}$	$5.54 \times 10^{25}$
ms900p	$900\pi$	17.0	$1.97 \times 10^3$	0.05	$4.73 \times 10^{30}$	$1.20 \times 10^{30}$	$1.06 \times 10^{26}$

tive motions after the formation of the PNS (e.g., Epstein 1979; Burrows & Lattimer 1988; Keil et al. 1996). It is not fully discussed whether the structure and coherency of the fossil magnetic field are retained in such a tumultuous situation. At least, independent from the spin rate of the PNS, the turbulent convection would strongly disturb, locally amplify, and transport the fossil field (Nordlund et al. 1994), unless the field strength is stronger than the equipartitioned one. The characteristics of the fossil field acquired before core-collapse thus seems likely to be lost during the evolution of the PNS. On the flip side, in the dynamo hypothesis, the convective motion would play a vital role in generating the large-scale magnetic field in the PNS. Its importance is indisputable.

The convective dynamo in the PNS is discussed in TD93 theoretically under the modern scenario of the core-collapse supernova. In the context of the  $\alpha$ - $\Omega$  dynamo (e.g., Parker 1955), they argue that a large-scale magnetic field with  $\mathcal{O}(10^{15})$  G, is generated when the spin period of the PNS ( $\equiv P_{\text{rot}}$ ) is shorter than  $\mathcal{O}(10)$  ms. This constraint comes from the prerequisite for operating the large-scale convective dynamo (e.g., Moffatt 1978; Krause & Raedler 1980): *the Rossby number should be smaller than unity*, that is  $Ro \equiv v / (2\Omega l) \lesssim 1$ , where the spin rate  $\Omega$ , the typical velocity and length-scale  $v$  and  $l$  with their chosen values  $v \simeq \mathcal{O}(10^3)$  km/s and  $l \simeq \mathcal{O}(0.1)$  km, corresponding to the convection velocity and scale-height expected in the outer region of the PNS. In the ordinary PNS with  $P_{\text{rot}} \gtrsim \mathcal{O}(10)$  ms (e.g., Ott et al. 2006), the large-scale magnetic field does not grow and the small-scale ‘‘patchy’’ magnetic structures would prevail. This is the standard, but still rough, framework they constructed for the PNS dynamo.

The numerical modeling is a powerful tool to refine the PNS dynamo theory. Bonanno et al. (2003) is the first to study the dynamo process in the PNS in the framework of the mean-field approximation. They have solved a mean-field induction equation with given pro-

files of turbulent electro-motive force and differential rotation without solving the development of the flow field. Then, they showed that the mean-field dynamo process would be effective for the most of the PNS (see also, Bonanno et al. 2006). Rheinhardt & Geppert (2005) studies the ability of the PNS convection to excite the dynamo with considering actual convection profiles taken from hydrodynamic simulations of rotating PNSs, and then shows that the geometrical structures of the velocity fields they employed are well suited to amplify a seed magnetic field. More recently, a groundbreaking study for the PNS dynamo was conducted by Raynaud et al. (2020). They have performed anelastic MHD simulations of the PNS dynamo under a realistic setup and then confirmed, for the first time, that the large-scale convective dynamo successfully occurs in the rapidly-rotating PNS, as predicted by TD93.

Although significant progress has been made in the study of the PNS dynamo with the development of the numerical method and the improved computing performance, the origin of the diversity of NS’s magnetic fields remains to be solved. ‘‘What physics is responsible for the diversity of NS’s magnetic fields?’’. To answer this question, we join the effort of the numerical modeling of the PNS dynamo. The aim of our study is to give shape to the theory of the PNS convection and dynamo in a more quantitative, self-consistent manner with the aid of numerical simulation. As a first step towards it, we construct a ‘‘PNS in a box’’ simulation model with solving the compressible magneto-hydrodynamics (MHD) with a nuclear EOS and a simplified leptonic transport process. Our simulation model has an ability to study various types of the PNS structure from spherical-shell convection states to full-sphere convection state. As a demonstration of our newly-developed model, here we study convection and dynamo processes in two-types of PNSs with different internal structure: one is in a fully-convective state and the other has a spherical shell convection state. The internal structures

of the PNS models are taken from core-collapse simulations, thus are more or less realistic. The dependence on the spin rate of the properties of the PNS dynamo is also studied by varying it systematically.

The outline of this paper is as follows. In § 2 we present the numerical model we constructed and simulation setups. The results obtained by the simulation run for models with different depths of the convection zone (CZ) and various spin rates are presented, with special focuses on the profiles of large-scale fields developed in models, in § 3. The spin-rate dependence of the dynamo activity and its relationship with the turbulent electro-motive force are discussed in § 4. We summarize and discuss the implications of our results in § 5.

## 2. SIMULATION MODEL

It is well known that the width of the CZ in the PNS changes depending not only on the physical properties of the progenitor star (e.g., Nagakura et al. 2019; Torres-Forné et al. 2019) but also on the evolution phase of the PNS (e.g., Keil et al. 1996; Pons et al. 1999; Roberts et al. 2012; Camelio et al. 2019). Since the CZs with various depths are expected to develop in the interior of the PNS, the numerical model should have an ability to examine them comprehensively. To understand the origin of the diversity of the NS's magnetic fields, we construct a kind of “star in a box” simulation model (Freytag et al. 2002; Dobler et al. 2006; Käpylä 2020).

To cover the whole sphere from the center to pseudo-surface, the PNS is described as a spherical sub-region of radius  $R_{\text{PNS}}$  of a cubic box of size  $L_{\text{box}}^3$  and is solved in the Cartesian grids  $(x, y, z)$ . The spherical coordinates  $(r, \theta, \phi)$  are used for analysis. The baryonic matter in the box is governed by fully-compressible non-relativistic MHD equations. The general relativistic effects are not taken into consideration in this work. The leptonic transport which characterizes the PNS is additionally solved under the diffusion approximation. Basic equations are written, in a rotating reference frame with an angular velocity  $\Omega_0$ , as

$$\frac{D\rho}{Dt} + \rho \nabla \cdot \mathbf{v} = 0, \quad (1)$$

$$\begin{aligned} \frac{D\mathbf{v}}{Dt} = & -2\Omega_0 \mathbf{e}_z \times \mathbf{v} - \frac{1}{\rho} \nabla P + \frac{1}{4\pi\rho} (\nabla \times \mathbf{B}) \times \mathbf{B} \\ & + \frac{2}{\rho} \nabla \cdot (\rho\nu\mathbf{S}) + \mathbf{g} + \mathbf{f}_{\text{damp}}, \end{aligned} \quad (2)$$

$$\begin{aligned} \frac{D\epsilon}{Dt} = & -\frac{P\nabla \cdot \mathbf{v}}{\rho} + 2\nu\mathbf{S}^2 \\ & + \frac{\eta(\nabla \times \mathbf{B})^2}{4\pi\rho} + \frac{\gamma\nabla \cdot (\kappa\nabla\epsilon)}{\rho} + \dot{\epsilon}_{\text{damp}} \end{aligned} \quad (3)$$

$$\frac{\partial \mathbf{B}}{\partial t} = \nabla \times (\mathbf{v} \times \mathbf{B} - \eta \nabla \times \mathbf{B}), \quad (4)$$

$$\frac{DY_e}{Dt} = \nabla \cdot (\xi \nabla Y_e) + \dot{Y}_{e,\text{source}}, \quad (5)$$

with the strain rate tensor

$$S_{ij} \equiv (\partial_j v_i + \partial_i v_j - 2\delta_{ij} \partial_i v_i / 3) / 2, \quad (6)$$

where  $\epsilon$  is the specific internal energy,  $Y_e$  is the lepton fraction,  $\gamma$  is the adiabatic index, and the other symbols have their usual meanings. The viscous, magnetic, heat, and lepton diffusivities are given by  $\nu$ ,  $\eta$ ,  $\kappa$  and  $\xi$ , respectively. To avoid boundary artifacts, the damping terms  $\mathbf{f}_{\text{damp}}$  and  $\dot{\epsilon}_{\text{damp}}$  are added to eqs. (2) and (3), which keep  $\mathbf{v}$  and  $\epsilon$  outside the PNS close to the initial profiles, and are given by

$$\mathbf{f}_{\text{damp}} = -\frac{\mathbf{v}}{\tau_d} f_{\text{ext}}, \quad \dot{\epsilon}_{\text{damp}} = \frac{\epsilon_{\text{ini}} - \epsilon}{\tau_d} f_{\text{ext}}, \quad (7)$$

with

$$f_{\text{ext}} = \frac{1}{2} \left[ 1 + \tanh \left( \frac{r - R_d}{w_t} \right) \right], \quad (8)$$

where  $\epsilon_{\text{ini}}$  is the initial profile of  $\epsilon$ ,  $R_d$  is the damping radius,  $\tau_d$  is the damping time and  $w_t$  is the width of the transition layer between the PNS and the “buffer” damping region. For maintaining the lepton gradient, the source term is added to the lepton transport equation

$$\dot{Y}_{e,\text{source}} = \frac{Y_{e,\text{ini}} - Y_e}{\tau_s} f_{\text{int}} \quad (9)$$

with

$$f_{\text{int}} = \frac{1}{2} \left[ 1 - \tanh \left( \frac{r - R_d}{w_t} \right) \right], \quad (10)$$

where  $Y_{e,\text{ini}}$  is the initial profile of  $Y_e$ , and  $\tau_s$  is the forcing time. This is a simple model for the replenishment of the lepton via the energy conversion from the gravity to the neutrino radiation inside the PNS during its cooling time<sup>1</sup>. To close the system, we employ the EOS by Latimer & Swesty (1991) with a compressibility modulus of  $K = 220$  MeV.

We set up two-types of initial equilibrium models as typical examples for our newly-developed code : *model* mf is based on a post-bounce core (about 100 ms after the core bounce) from a hydrodynamic simulation of “rotating” core-collapse of  $15M_{\odot}$  progenitor and *model* ms is based on a post-bounce core (about 600

<sup>1</sup> Our PNS dynamo simulations focus on the timescales of less than “300 ms”, which is shorter than typical thermodynamic evolution time of the PNS (e.g.,  $\sim 1000$  ms in Scheck et al. (2006) for the standard case). On such timescale, the behavior of neutrino transport is expected to be similar to (not so different from) that in the condition adopted as our initial setup. Hence, we models the lepton-driven convection by adding the forcing term, that can maintain the initial profile of the lepton fraction moderately, to the lepton transport equation.

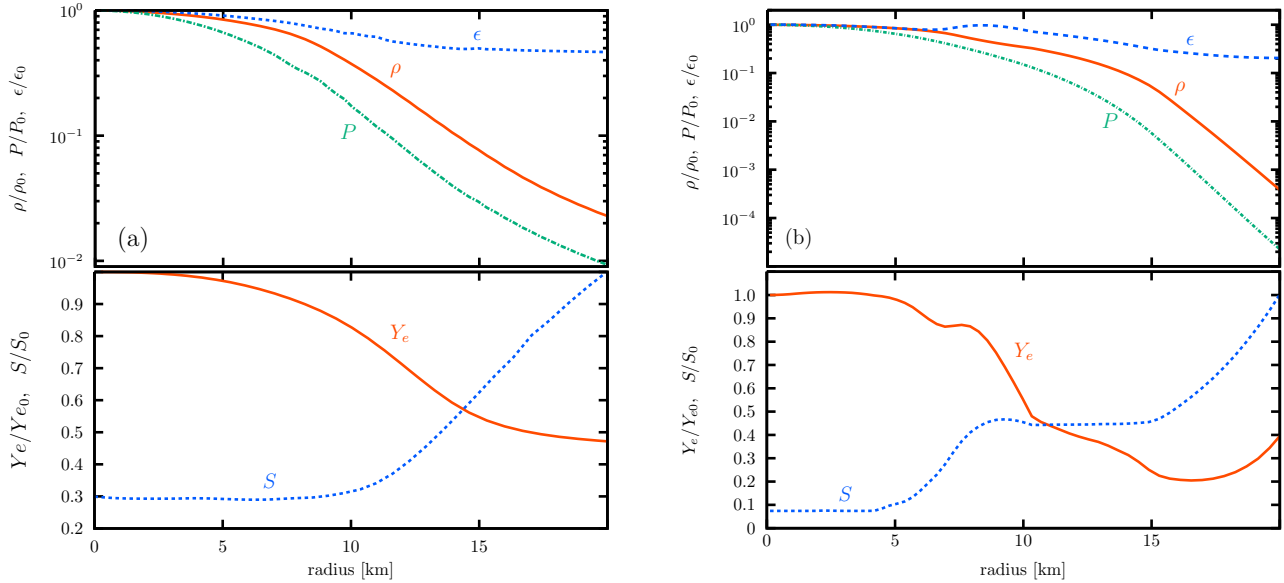


**Figure 1.** Radial distributions of  $\rho$ ,  $P$ ,  $\epsilon$  (top), and  $Y_e$ ,  $S$  (bottom) for (a) full-sphere convection model (*model mf*) and (b) spherical-shell convection model (*model ms*). Normalizations are  $\rho_0 = 2.5 \times 10^{14}$  g/cm<sup>3</sup>,  $P_0 = 5.86 \times 10^{33}$  dyn/cm<sup>2</sup>,  $\epsilon_0 = 5.85 \times 10^{19}$  erg/g,  $Y_{e0} = 0.35$ , and  $S_0 = 3.96k_B$  for *model mf*,  $\rho_0 = 6.23 \times 10^{14}$  g/cm<sup>3</sup>,  $P_0 = 5.54 \times 10^{34}$  dyn/cm<sup>2</sup>,  $\epsilon_0 = 8.15 \times 10^{20}$  erg/g,  $Y_{e0} = 0.27$ , and  $S_0 = 6.51k_B$  for *model ms*.

ms after the bounce) of “non-rotating” core-collapse of  $11.2M_\odot$  progenitor. In both models, the shock wave has reached  $\sim 200$  km, and the PNSs are settled into a quasi-hydrostatic state. The hydrodynamic variables and gravitational potential within  $0 \leq r \leq 20$  km ( $\equiv L_{\text{box}}/2$ ) are extracted, and then the PNS is reconstructed with a 2nd-order interpolation method in the calculation domain ranging  $-L_{\text{box}}/2 \leq x, y, z \leq L_{\text{box}}/2$ .

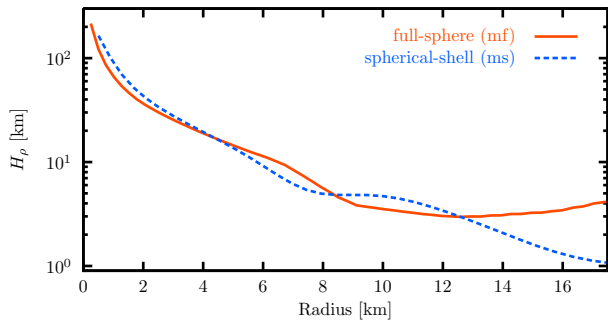


**Figure 2.** Radial distribution of the density scale-height ( $H_\rho \equiv -dr/d\ln\rho$ ) for *model mf* (red-solid) and *model ms* (blue-dashed).

Shown in Figure 1 is the initial profile of the hydrodynamic variables for (a) *model mf* and (b) *model ms*. While the profiles of  $\rho$ ,  $P$ , and  $\epsilon$  are shown in top panels,  $Y_e$  and  $S$  (entropy) are in bottom panel in each figure. The radial profile of the density scale-height  $H_\rho$  for each model is also shown in Figure 2. There is no significant difference in the profile of  $H_\rho$  between two models. How-

ever, there are remarkable differences in the profiles of  $Y_e$  and  $S$  between models. For *model mf*, while the negative lepton gradient which lies in the inner part of the PNS powers the lepton-driven convection (e.g., Epstein 1979; Keil et al. 1996), the outer region where  $r \gtrsim 15$  km is stable to the convective instability based on the Ledoux criterion (e.g., Ledoux 1947; Kippenhahn, & Weigert 1990). In contrast, for *model ms*, the possible site for the lepton-driven convection is confined in the layer in the range  $7.5\text{km} \lesssim r \lesssim 15$  km, while the inner core and outer envelope are convectively stable due to the positive entropy gradient. In this paper, to explore the response of the PNS convection and dynamo to the spin rate, we vary the magnitude of  $\Omega_0$  in two models while keeping the background hydrostatic state unchanged. We investigate the cases with  $\Omega_0 = 12\pi, 60\pi$  and  $120\pi$  for *model mf* and the cases with  $\Omega_0 = 100\pi, 300\pi$  and  $900\pi$  for *model ms*, respectively. See the summary of the simulation run in Table 1.

Since the outer convectively stable layer has less impact on the hydrodynamics of the PNS during the evolution time of interest ( $\mathcal{O}(100)$  ms), the damping radius is chosen as  $R_d = 17.5$  km so that the pseudo-surface of the PNS would be  $R_{\text{PNS}} \simeq 15$  km. We connect the PNS to the outer buffer region through the transition layer with  $w_t = 0.05R_{\text{PNS}}$ . The forcing time for the lepton is assumed to be constant inside the PNS and an order of magnitude shorter than the typical convective turn-over time, that is  $\tau_s = 0.1\tau_{\text{cv}}$ , where  $\tau_{\text{cv}} \equiv l_{\text{sh}}/v_{\text{cv}}$  with the typical convection velocity  $v_{\text{cv}} = 10^8$  cm/s and

the typical scale-height  $l_{\text{sh}} = 10^5$  cm. With this value, we can keep the profile of  $Y_e$  close to, but slightly deviate from, the initial state. To reduce the boundary artifacts as much as possible, we adopt a short damping time of  $\tau_d = 0.1\tau_s$ . We choose, as a first step, uniform diffusivities of  $\nu = \eta = \kappa = \xi = 10^{11}$  cm<sup>2</sup>/s inside the PNS. While  $\nu$ ,  $\kappa$  and  $\xi$  assumed here are within the expectations in the PNS<sup>2</sup>,  $\eta$  is far from realistic value ( $\eta_{\text{PNS}} \sim 10^{-5}$  cm<sup>2</sup>/s) (e.g., Rheinhardt & Geppert 2005; Masada et al. 2007) because of a numerical limitation as is so often the case with the planetary and stellar dynamo simulations (e.g., Jones 2011; Brun & Browning 2017).

The governing equations are solved by the second-order Godunov-type finite-difference scheme which employs an approximate MHD Riemann solver (see Sano et al. 1999; Masada et al. 2012, 2015, for details). The calculation domain is resolved by  $N^3 = 256^3$  grid points. After a random small “seed” magnetic field with the amplitude  $|\delta B| < 10^9$  G is introduced into the CZ of the PNS, the calculation is started by adding a small perturbation to the initial pressure distribution for both models. Note that, in this paper, the simulation is terminated when the calculation time exceeds roughly 250 ms, with taking into account that the structure of the PNS can change in about a few hundred milli-seconds as the neutrino radiation proceeds (e.g., Keil et al. 1996; Scheck et al. 2006; Nagakura et al. 2019).

In the following, to examine the convective and magnetic structures in detail, we define the following three averages of a function  $h(r, \theta, \phi)$ .

The volume average over the entire CZ:

$$\langle h \rangle_V \equiv \int h(r, \theta, \phi) dV_{\text{CZ}} / \int dV_{\text{CZ}}, \quad (11)$$

where  $V_{\text{CZ}}$  is the volume of the CZ.

The longitudinal average:

$$\langle h \rangle_\phi = \frac{1}{2\pi} \int_{-\pi}^{\pi} h(r, \theta, \phi) d\phi. \quad (12)$$

The spherical average:

$$\langle h \rangle_s = \frac{1}{4\pi} \int_{-1}^1 \int_{-\pi}^{\pi} h(r, \theta, \phi) d\cos\theta d\phi. \quad (13)$$

The time-average of each spatial mean is denoted by additional angular brackets, such as  $\langle\langle h \rangle_\theta \rangle$ .

<sup>2</sup> In the PNS below the neutrinosphere, the neutrino diffusion process controls the magnitude of the diffusion coefficients, except the magnetic diffusivity (Thompson & Duncan 1993).

### 3. RESULTS

#### 3.1. Temporal Evolution and Convection Profiles

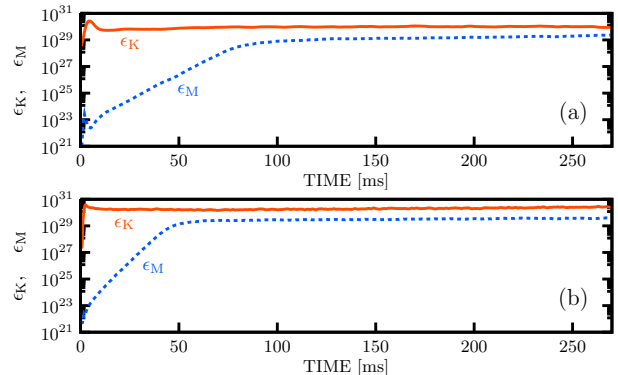


**Figure 3.** Temporal evolution of  $\epsilon_K$  (red-solid) and  $\epsilon_M$  (blue-dashed) for (a) *model mf* and (b) *model ms*.

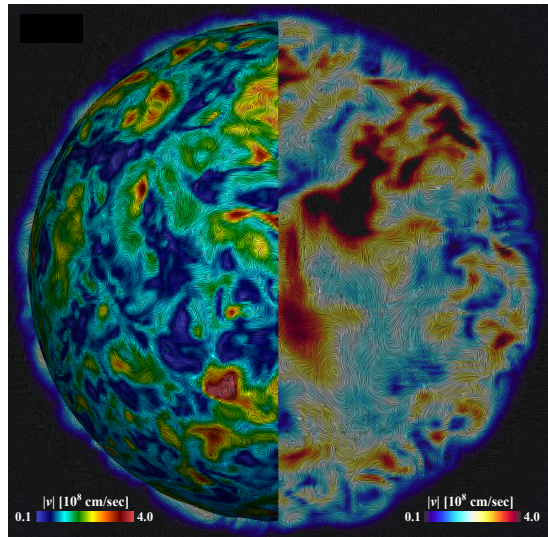


**Figure 4.** LIC visualizations of  $|\mathbf{v}|$  at  $r = 15$  km (left hemisphere) and meridional cutting plane (right hemisphere) when  $t = 230$  ms for *model mf12p* as a demonstration. Normalization unit is  $10^8$  cm/s. Red (blue) tone denotes higher (lower) convection velocity.

The rough sketch of the simulation results is summarized. The typical temporal evolution of the volume-averaged kinetic and magnetic energies ( $\epsilon_K$  and  $\epsilon_M$ ) for (a) *model mf* (mf12p) and (b) *model ms* (ms100p) is shown in figure 3, where  $\epsilon_K \equiv \langle \rho \mathbf{v}^2 / 2 \rangle_V$  and  $\epsilon_M \equiv \langle \mathbf{B}^2 / (8\pi) \rangle_V$ . The volume-average is taken over the entire CZ. When the simulation proceeds, the lepton-driven convection begins to grow and then both kinetic and magnetic energies are amplified in the PNS. The kinetic energy saturates within  $\sim 50$  ms. At the saturated stage, the turbulent convection motion dominates

the PNS as shown in figure 4 where the structure of the convection on the PNS surface (left hemisphere) and the meridional cutting plane (right hemisphere) for *model* mf (mf12p) is visualized as a demonstration. In contrast, the magnetic energy gradually increases and reaches a quasi-steady state after  $t = 150 \sim 200$  ms in both models. Since the convective turn-over time is longer in *models* mf than in *models* ms due to the larger scale-height in the deeper CZ, it takes longer time for the magnetic energy to be amplified. The saturation level of the magnetic energy is below that of the convective kinetic energy, suggesting that the MHD dynamos operated in our models are in a turbulent regime rather than a magneto-strophic regime (e.g., Brun & Browning 2017; Raynaud et al. 2020). See Table 1 for more details on the temporal means of  $\epsilon_K$  and  $\epsilon_M$  for each model.

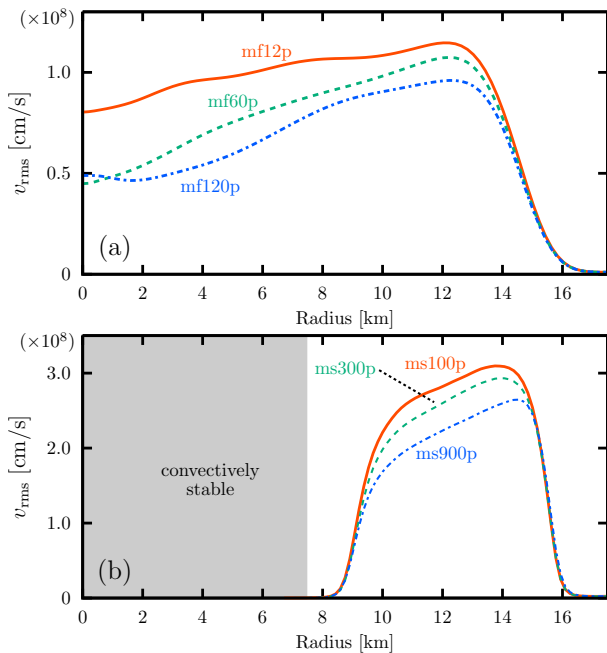


**Figure 5.** Radial profiles of  $v_{\text{rms}}$  for (a) *models* mf and (b) *models* ms at the equilibrated stage. The different line types correspond to the models with different spin rates in each panel.

The radial profiles of  $v_{\text{rms}}$  at the saturated stage for models (a) mf and (b) ms are shown in figure 5, where  $v_{\text{rms}}$  is the RMS of the perturbed radial velocity defined by  $v_{\text{rms}} \equiv \langle \langle (v_r - \langle v_r \rangle_\phi)^2 \rangle_s^{1/2} \rangle$ . The different line types correspond to the models with different spin rates. The shaded region in panel (b) denotes the convectively-stable region.

Overall, the convection velocity is an order of  $10^8$  cm/s although it is a few times higher in *models* ms than in *models* mf because of the larger thermal energy stored in *model* ms at the initial setup stage (See, fig. 1). Since

the rotational constraint, caused by the Coriolis force, on the convective motion becomes stronger in the model with the higher spin rate, the convection velocity decreases as the spin rate increases, which can be seen in each model (See, Table 1).

As a corollary of the turbulent convective motion regulated by the rotation, large-scale flow, thermodynamic and magnetic structures are built up in the PNS. In the following, we will discuss in detail the results obtained with each model.

### 3.2. Models mf : Full-sphere Convection Models

#### 3.2.1. Mean Flow and Thermodynamic Fields

Meridional distributions of (a)  $\langle \langle v_\theta \rangle_\phi \rangle$ , (b)  $\delta\epsilon \equiv \langle \langle \epsilon - \langle \langle \epsilon \rangle_s \rangle \rangle_\phi$  and (c)  $\Omega \equiv \langle \langle v_\phi \rangle_\phi \rangle / r \sin \theta + \Omega_0$  are shown in Figure 6. The overplotted arrows in panel (a) are meridional velocity vectors with arbitrary amplitudes. Panels (a1)–(c1) are for mf12p, (a2)–(c2) are for mf60p, and (a3)–(c3) are for mf120p, respectively.

From the symmetry point of view, the large-scale flows seen in *models* mf can be divided into two types : (i) a single-cell meridional circulation with a north-south anti-symmetric differential rotation (mf12p), and (ii) a double-cell meridional circulation (single-cell per hemisphere) with a cylindrical differential rotation (mf60p and mf120p). While the dipole dominance in  $\delta\epsilon$  is accompanied with the flow pattern (i), it can be seen that the quadrupolar dominance in  $\delta\epsilon$  is developed in conjunction with the pattern (ii).

The single-cell counter-clockwise profile with circulating between northern and southern hemispheres, seen in fig.6(a1), should be due to the very slow spin of mf12p. As shown in Chandrasekhar (1961) (see § 59), the dipole dominance of the convective flow is a natural topological result of the full-spherical convection domain. See § 3.3.1 for related discussion. Since the northern and southern hemispheres are dominated respectively by cool (and fast) down-flow and warm (and slow) up-flow, the large-scale coherent circulation in-between them is formed, resulting in the anti-symmetric profile of  $\delta\epsilon$  with respect to the equator (see fig.6(b1)). The difference of  $\delta\epsilon$  between hemispheres is averagely  $4 \times 10^{17}$  erg/g which provides  $10^{50} - 10^{51}$  erg when considering the total mass of the PNS.

The profile of  $\Omega$  for mf12p (fig.6(c1)) should be determined to retain a quasi-steady convective state: the production of vorticity by the baroclinic term ( $\propto \partial \bar{\epsilon} / \partial \theta$ ) should be balanced mainly with the production of relative vorticity by the stretching ( $\propto \partial \Omega / \partial z$ ), that is, the thermal wind balance

$$\frac{\partial \omega}{\partial t} = r \sin \theta \frac{\partial \Omega^2}{\partial z} - \frac{g}{\gamma \bar{\epsilon}} \frac{\partial \bar{\epsilon}}{\partial \theta} \dots = 0, \quad (14)$$

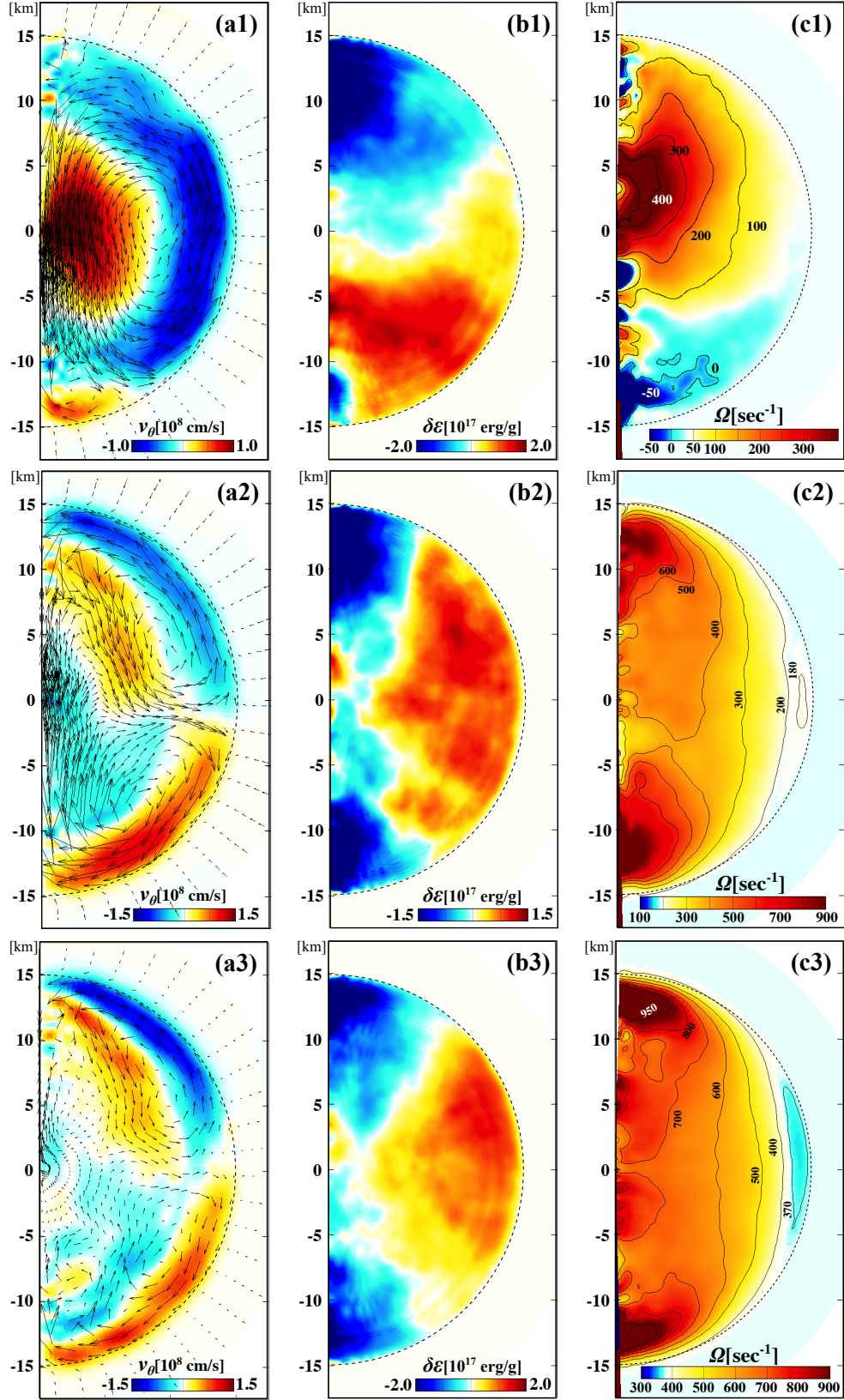


**Figure 6.** Meridional distributions of (a)  $\langle v_\theta \rangle_\phi$ , (b)  $\delta\epsilon$  and (c)  $\Omega$  for *model* mf. The top, middle and bottom panels are corresponding to *models* mf12p, mf60p, and mf120p, respectively. In panel (a), the streamlines are overplotted with an arrow length proportional to the flow velocity. In panel (c), the region rotating with the reference frame  $\Omega_0$  is shown by white color. The iso-rotation contours are also overplotted.

should be maintained to retain the steady state, where  $\omega$  is the vorticity and  $\bar{\epsilon}$  is the time and azimuthally-averaged specific internal energy. Note that this equation can be obtained as the meridional component of the mean-field equation of motion (see, e.g., Pedlosky 1982; Masada 2011).

Eq.(14) predicts that the latitudinal variation of  $\bar{\epsilon}$  produces a change of  $\Omega$  in the  $z$ -direction. Since  $\partial\bar{\epsilon}/\partial\theta \gtrsim 0$  over the entire CZ in mf12p, the spin rate should increase in the  $z$ -direction to satisfy eq.(14). This is qualitatively consistent with what we observe in mf12p, i.e., differential rotation with a north-south anti-symmetry, which progrades in the north and retrogrades in the southern hemisphere of the PNS (see fig.6(c1)). The overall mean properties of the hydrodynamics seen in mf12p are analogous to those in Brun & Palacios (2009) (see their model labeled RG2) though their simulated object is the red giant which is different from us.

The profile of the meridional flow seen in *models* mf60p and mf120p consists of a double-cell circulation (single-cell per hemisphere (see fig.6(a2) or (a3)). While it is poleward at the upper CZ, it reverses to an equatorward direction at deeper depths. In such a case, the polar and equatorial regions are dominated respectively by cool down-flow and warm up-flow, naturally resulting in the quadrupolar structure of the thermodynamic field seen in the profile of  $\delta\epsilon$  (fig.6(b2) or (b3)). This type of circulation flow is often seen in convection simulations of slowly-rotating solar-type stars with thin CZs (e.g., Mabuchi et al. 2015). The driving mechanism of such a double-cell circulation (single-cell per hemisphere) will be discussed in detail in § 3.3.1 because the similar profile can be observed even in *models* ms.

A remarkable property of the differential rotation achieved in mf60p and mf120p is that it is almost invariant along the rotation axis, i.e.,  $\partial\Omega/\partial z \simeq 0$  (see fig.6(c2) or (c3)). It is well-known that, according to the Taylor-Proudman constraint, the fluid parcel tends to move and thus its velocity to be uniform along the rotation axis in the system with sufficiently large Coriolis force (Pedlosky 1982; Kitchatinov & Ruediger 1995; Brun & Toomre 2002; Miesch et al. 2006; Masada 2011). The latitudinal variation of  $\Omega$  is the anti-solar type, that is the spin rate is lower at the equator than in the polar regions. The anti-solar type differential rotation is also a characteristic feature of the relatively slowly spinning system. It should be noted that the overall mean flow properties in mf60p and mf120p are also analogous to those in Brun & Palacios (2009) (see their model labeled RG1) where the deep core convection in the red-giant is discussed.

### 3.2.2. Magnetic Field : Dynamo Activities

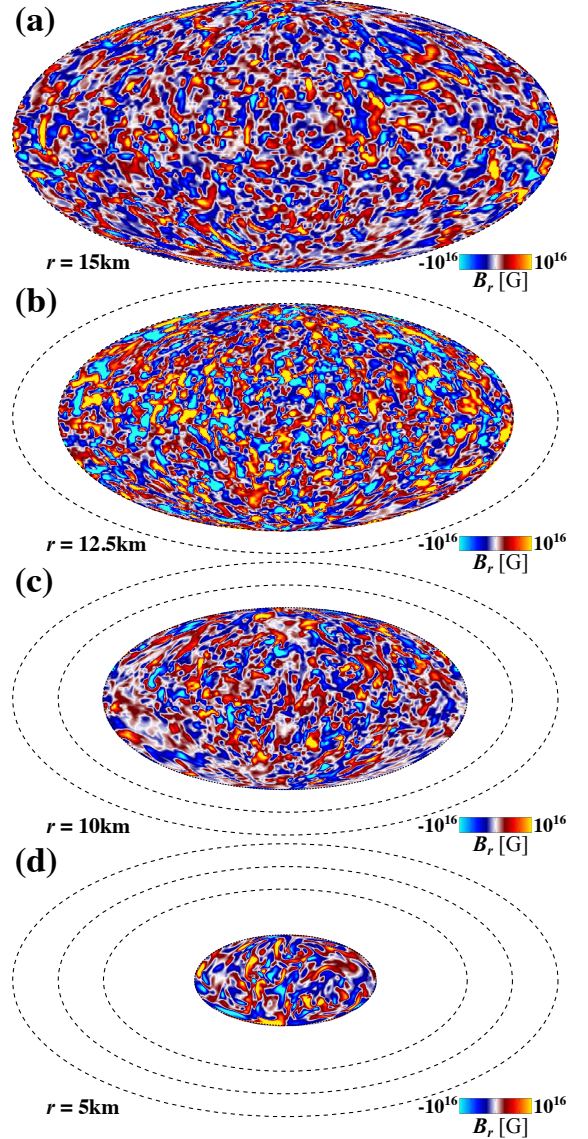


**Figure 7.** Distributions of the radial component of the magnetic field on spherical surfaces at sampled radii  $r = 15\text{km}$ ,  $12.5\text{km}$ ,  $10\text{km}$ , and  $5\text{km}$  when  $t = 230\text{ms}$  in the Mollweide projection for *model* mf (mf12p) as a reference.

The magnetic field which is amplified by the PNS convection shows a complicated structure mixed with the turbulent and large-scale components. Primarily, the turbulent convective motion produces small-scale intense magnetic fields. Figure 7 shows, as a demonstration, the distribution of the radial component of the magnetic field on spherical surfaces at different depths for mf12p in the Mollweide projection. The red (blue) tone denotes the positive (negative) value of the field strength. It is found that the turbulent component of

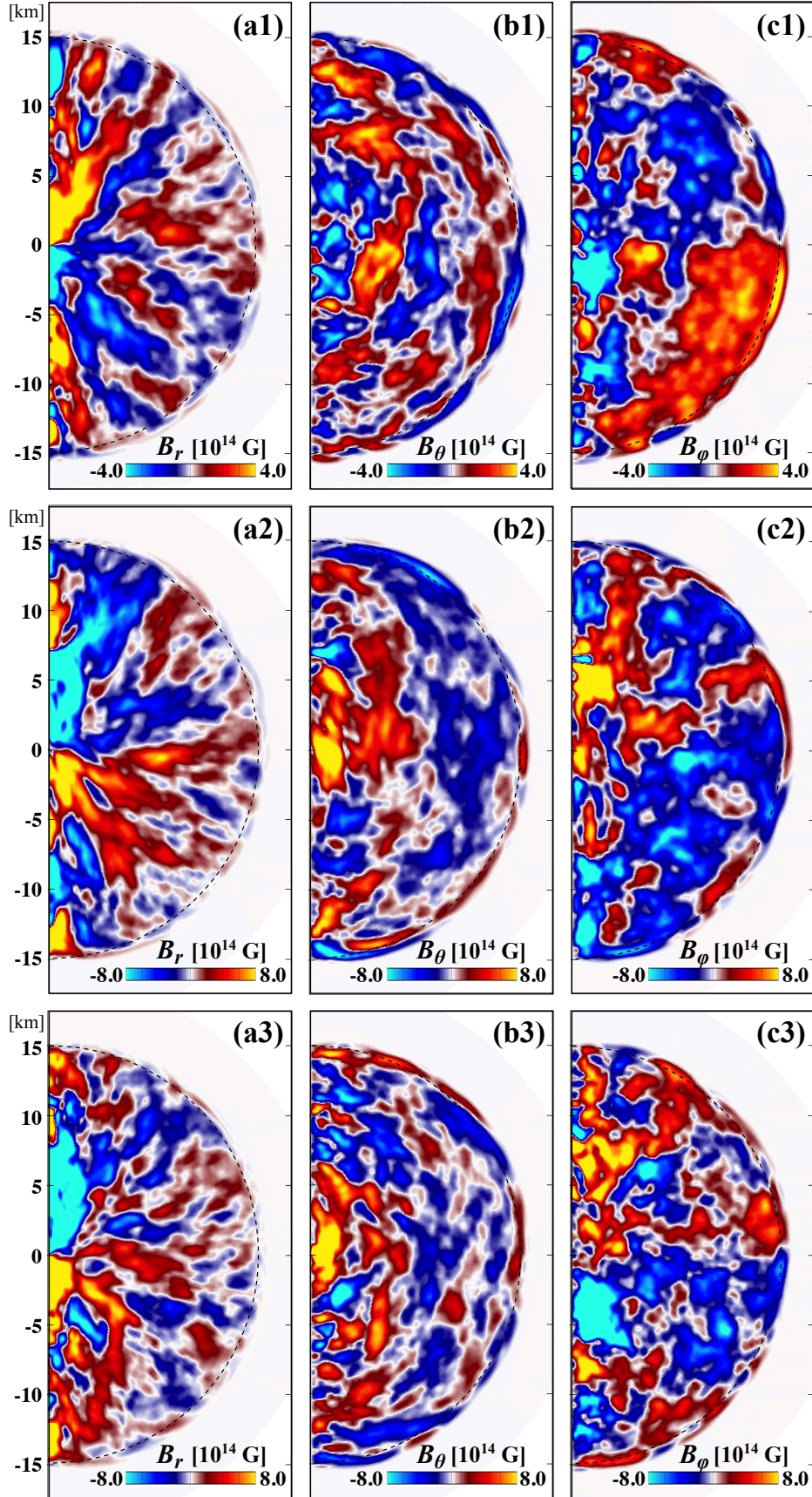


**Figure 8.** Meridional distributions of large-scale magnetic components, (a)  $\langle\langle B_r \rangle\rangle$ , (b)  $\langle\langle B_\theta \rangle\rangle$  and (c)  $\langle\langle B_\phi \rangle\rangle$  for *model* mf. The top, middle and bottom panels are corresponding to *models* mf12p, mf60p, and mf120p, respectively. The time average is taken over the duration  $220 \leq t \leq 240$  ms.

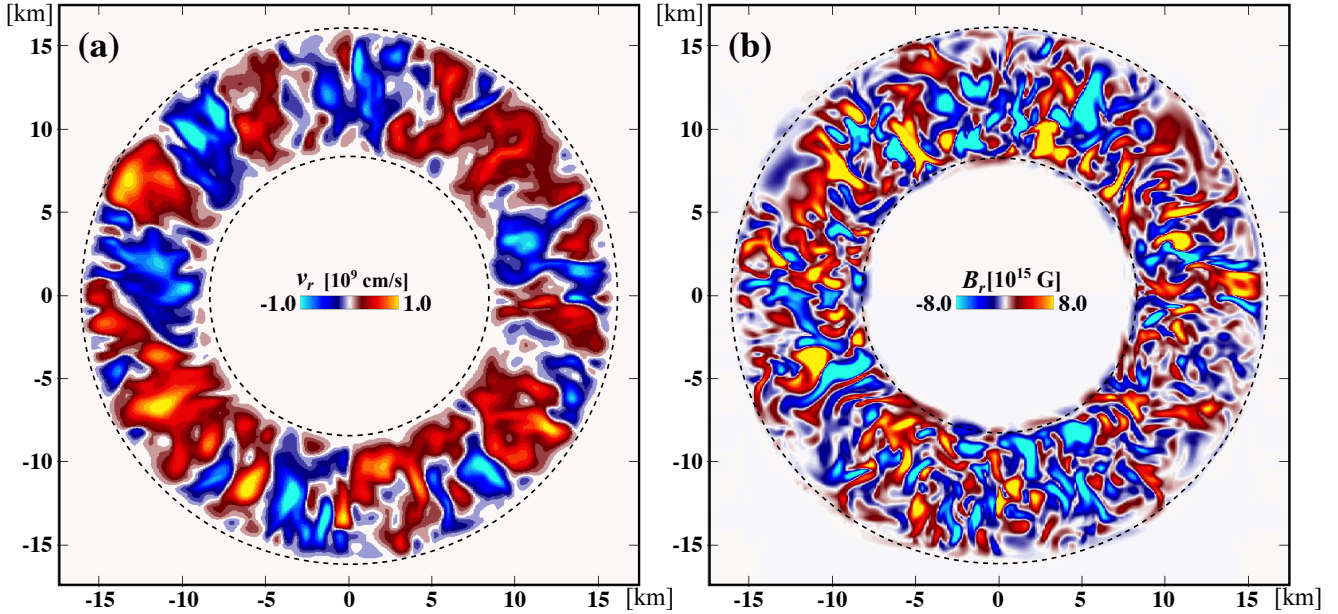


**Figure 9.** Instantaneous snapshots for the distributions of (a)  $v_r$  and  $B_r$  when  $t = 220$  ms for *model ms* (ms100p) at the meridional cutting plane. The red (blue) tone denotes the positive (negative) values.

the magnetic field becomes predominant inside the PNS. It is amplified via small-scale convective dynamo (e.g., Cattaneo 1999; Schekochihin et al. 2004) and finally reaches to the strength of  $\mathcal{O}(10^{16})$  G, which contains the energy of about 30 % of the convective kinetic energy at the saturated stage (see, fig.3 and Table 1). Turbulent magnetic components show similar characteristics in other full-sphere convection models, i.e., mf60p and mf120p.

In such a haystack of turbulent magnetic components, the large-scale magnetic structure is spontaneously organized in *models mf*. Shown in figure 8 is the meridional distributions of large-scale magnetic components, (a)  $\langle\langle B_r \rangle\rangle_\phi$ , (b)  $\langle\langle B_\theta \rangle\rangle_\phi$  and (c)  $\langle\langle B_\phi \rangle\rangle_\phi$  for *models mf*. The top, middle and bottom panels are corresponding to *models mf12p*, *mf60p*, and *mf120p*, respectively. The time average is taken over the duration  $220 \leq t \leq 240$  ms. The red (blue) tone denotes the positive (negative) magnetic field strength.

Commonly, the global structure of the mean magnetic component exhibits a dipole dominance in these models. It can be found that the large-scale poloidal component, rooted deep in the central part of the PNS, shows a strong dipole symmetry, while it is less coherent in the outer part of the sphere. The strength of it reaches averagely  $\mathcal{O}(10^{14})$  G (locally exceeds  $10^{15}$  G), which is compatible with that expected in the strongly-magnetized NSs, so-called “magnetars” (e.g., Turolla et al. 2015; Enoto et al. 2019, and references therein). Additionally to the poloidal component, a large-scale toroidal magnetic component is also built up mainly in the outer part

of the PNS, especially in the relatively slowly-spinning models (mf12p and mf60p). It is roughly anti-symmetric with respect to the equator and also has an average strength of  $\mathcal{O}(10^{14})$  G, which is a bit weaker than the poloidal component.

The large-scale magnetic component observed in *models mf* would be the self-organized structure as a natural outcome of the symmetry breaking forced by the NS’s spin. Although the successful large-scale dynamo has been observed in a lot of solar, stellar, and planetary MHD convection simulations (e.g., Ghizaru et al. 2010; Käpylä et al. 2012; Masada et al. 2013; Fan & Fang 2014; Hotta et al. 2016)(See, Charbonneau 2020, for review), our intriguing finding here is that the large-scale field can be organized even in a relatively slow rotation regime than that predicted by TD93. The dependence of the large-scale magnetic field on the spin rate and the mechanism for the large-scale dynamo observed in our simulation models are discussed comprehensively in § 4.

### 3.3. *Models ms : Spherical-shell Convection Models*

#### 3.3.1. *Mean Flow and Thermodynamic Fields*

Unlike *models mf* with the full-sphere CZ, the turbulent convective motion is confined within the spherical-shell in *models ms* as presented in figure 9(a), where the instantaneous snapshot for the profile of  $v_r$  on a meridional cutting plane for ms100p is demonstrated. The convection velocity becomes maximum at the upper part of the CZ as shown in figure 2(b), and locally reaches  $\mathcal{O}(10^9)$  cm/s. The symmetry of the system is broken by the spinning motion of the PNS, resulting in

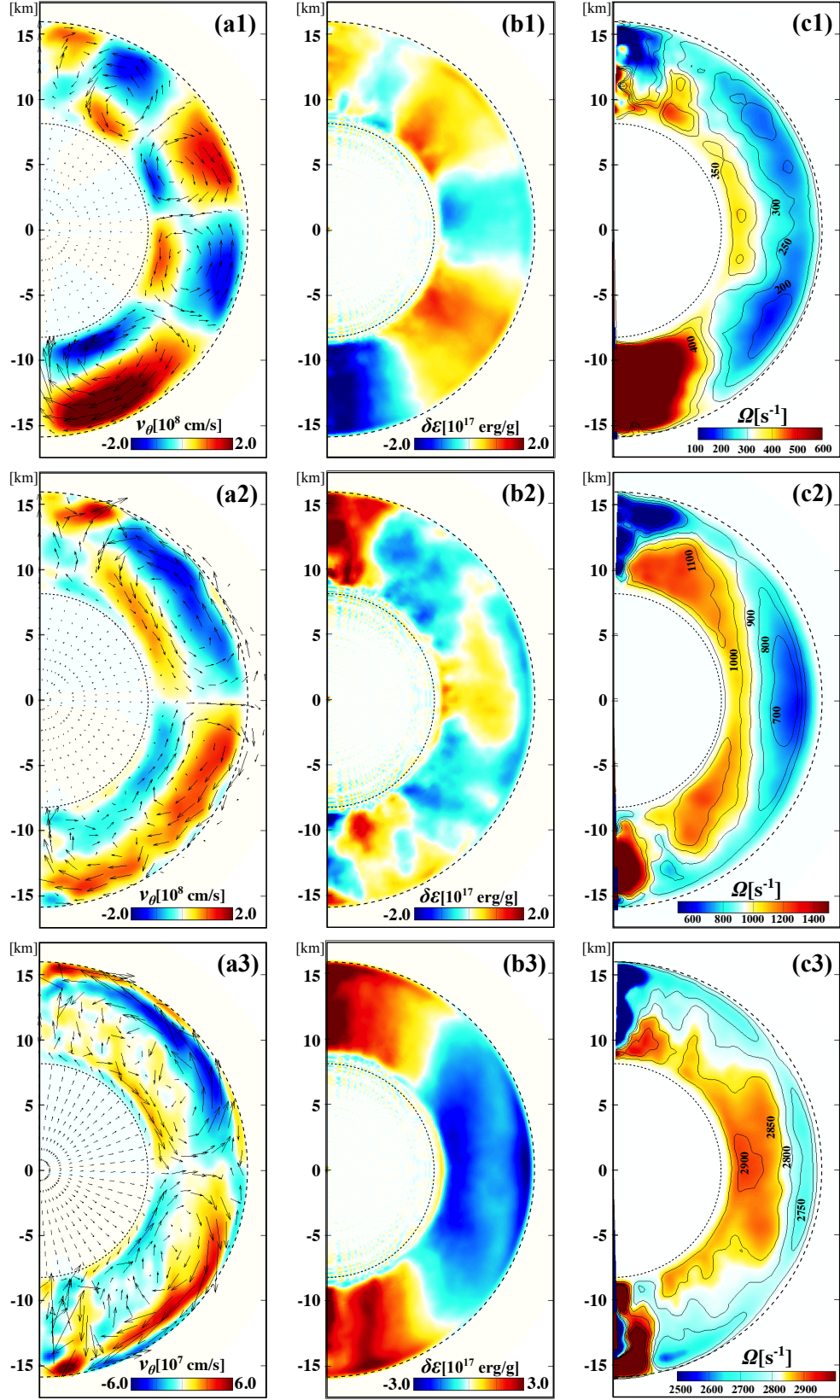


**Figure 10.** Meridional distributions of (a)  $\langle\langle v_\theta \rangle\rangle_\phi$ , (b)  $\delta\epsilon \equiv \langle\langle \epsilon - \langle\langle \epsilon \rangle\rangle_s \rangle\rangle_\phi$  and (c)  $\Omega \equiv \langle\langle v_\phi \rangle\rangle_\phi / r \sin \theta + \Omega_0$  for models ms. The top, middle and bottom panels are corresponding to models ms100p, ms300p, and ms900p, respectively. In panel (a), the streamlines are overplotted with an arrow length proportional to the flow velocity. In panel (c), the region rotating with the reference frame  $\Omega_0$  is shown by white color. The iso-rotation contours are also overplotted.

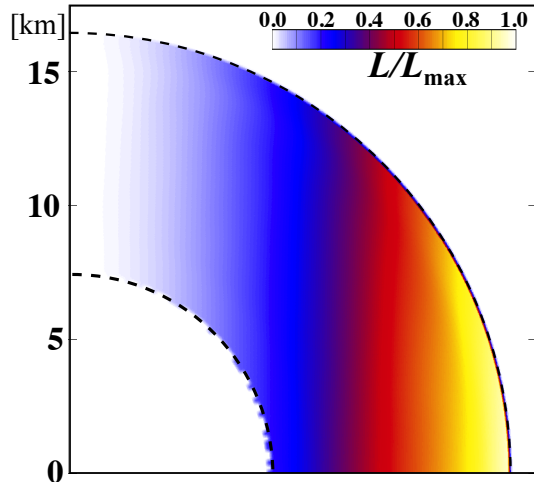


**Figure 11.** Meridional distribution of the normalized angular momentum,  $\mathcal{L} \equiv \varpi^2 \Omega$ , in the northern hemisphere for *models ms* (ms900p). The normalization unit is the maximum value of  $\mathcal{L}$  which corresponds to that in the equatorial surface.

an off-diagonal component of the Reynolds stress, which in turn gives rise to the mean flow and the large-scale thermodynamic structure even in *models ms*<sup>3</sup>.

Meridional distributions of (a)  $\langle \langle v_\theta \rangle_\phi \rangle$ , (b)  $\delta \epsilon \equiv \langle \langle \epsilon - \langle \langle \epsilon \rangle_s \rangle_\phi \rangle$  and (c)  $\Omega \equiv \langle \langle v_\phi \rangle_\phi \rangle / r \sin \theta + \Omega_0$  for *models ms* are shown in Figure 10. The overplotted arrows in panel (a) are meridional velocity vectors with arbitrary amplitudes. Panels (a1)–(c1) are for ms100p, (a2)–(c2) are for ms300p, and (a3)–(c3) are for ms900p, respectively.

From the symmetry point of view, the large-scale flows seen in *models ms* can be divided roughly into two types : (i) multi-cell meridional circulations with a shellular differential rotation (ms100p), and (ii) a double-cell meridional circulation (single-cell per hemisphere) with a cylindrical differential rotation (ms300p and ms900p). In ms100p with the lowest spin rate, the multi-polar structure of the thermodynamic field is developed due to the multi-cell circulation flow. On the other hand, the quadrupolar structure of the thermodynamic field, which is similar to that in mf60p and mf120p (see

<sup>3</sup> When the large-scale magnetic field grows, the magnetic braking may carry the angular momentum outside the CZ. However, as can be seen in Fig.6 or 10, there is no significant change in the angular velocity outside the CZ in our models. In our model, with taking account of the existence of the convectively stable layer surrounding the CZ in the PNS, we put the damping region outside the CZ. We control the flow velocity there to be almost the same as in the initial state (i.e.,  $\mathbf{v} = 0$ ), resulting in the redistribution of the angular momentum only inside the CZ.

figs.6(b2)and(b3)), can be observed in the models with relatively higher spin rates (ms300p and ms900p).

In the case of thin spherical-shell convection, like that operating in the Sun, it is well-known that the multi-cell pattern of the meridional flow is often observed in the faster rotation regime : the transition from the single-cell (per hemisphere) to multi-cell profiles of the circulation occurs when the spin rate increases (e.g., Feathstone & Miesch 2015; Mabuchi et al. 2015). However, intriguingly, our PNS models with the spherical-shell convection appear to show the opposite behavior : single-cell (per hemisphere) pattern appeared in faster rotating models (ms300p and ms900p), while the multi-cell in slowly-rotating model (ms100p).

The single-cell circulation (per hemisphere) can be qualitatively understood by the so-called “gyroscopic pumping” : when assuming the quasi-steady state, the equation for the conservation of angular momentum can be derived from the zonal component of the mean-field equation of motion as

$$\overline{\rho \mathbf{v}_M} \cdot \nabla \mathcal{L} = -\nabla \cdot \mathcal{F}_{RS}, \quad (15)$$

where the overbar denotes the time and longitudinal average,  $\mathbf{v}_M$  is the velocity of the meridional flow component,  $\mathcal{L} \equiv \varpi^2 \Omega = \varpi \langle \langle v_\phi \rangle_\phi \rangle + \varpi^2 \Omega_0$  is the specific angular momentum ( $\varpi = r \sin \theta$  is the cylindrical radius), and  $\mathcal{F}_{RS}$  is the turbulent angular momentum flux by the convective Reynolds stress which is described as

$$\mathcal{F}_{RS} \equiv \overline{\rho \varpi} \left( \overline{u'_r u'_\phi} \mathbf{e}_r + \overline{u'_\theta u'_\phi} \mathbf{e}_\theta \right). \quad (16)$$

Note that the other non-axisymmetric component of the stress, such as the Maxwell stress and molecular viscosity, are ignored because they are negligibly smaller than the Reynolds stress here.

Since the radial convection velocity is expected to be higher than the latitudinal and longitudinal velocities in a relatively-slow rotation regime, the angular momentum is transported mainly in the radially inward direction, that is  $\mathcal{F}_{RS} \propto \overline{u'_r u'_\phi} \mathbf{e}_r$  with  $\overline{u'_r u'_\phi} < 0$ . Then, the RHS of eq.(15) becomes positive (negative) in the upper (lower) CZ because  $\partial \mathcal{F}_{RS} / \partial r > 0$  ( $\partial \mathcal{F}_{RS} / \partial r < 0$ ) in the upper (lower) CZ when  $\mathcal{F}_{RS} = 0$  at the top and bottom boundaries (e.g., Miesch 2005; Miesch & Toomre 2009; Schrijver & Siscoe 2010).

On the other hand, the  $\mathcal{L}$  (specific angular momentum) has a cylindrical profile and decreases monotonically from equator to pole, that is  $\partial \mathcal{L} / \partial \theta < 0$  as shown in Figure 11 where the meridional distribution of the  $\mathcal{L}$  in the northern hemisphere of ms900p is demonstrated. Note that the similar profile of  $\mathcal{L}$  can be seen in ms300p. To retain the zonal momentum balance described by

eq.(15), the meridional flow should be poleward (i.e.,  $\bar{v}_\theta < 0$ ) in the upper CZ while it should be equatorward (i.e.,  $\bar{v}_\theta > 0$ ) in the lower CZ, providing the single-cell (per hemisphere) circulation flow seen in ms300p and ms900p. Note that the meridional flow observed in mf60p and mf120p should be driven by the same mechanism, that is the gyroscopic pumping.

The multi-cell pattern seen in ms100p (see fig.10(a1)) might be a consequence of the convective motion characterized by thick CZ, slow spin and relatively low Reynolds number. According to Chandrasekhar (1961) (§ 59), the spherical harmonic degree of the most unstable mode for the convective instability depends on the thickness of the CZ and becomes lower with the increase of it. The higher the spherical harmonic degree of the mode, the lower the growth rate becomes. At the limit of no rotation, the mode with  $l = 3-4$  seems to become the most unstable when the upper 40–60% of the sphere is convective. In the system with small Reynolds and Rayleigh numbers, such as those expected in PNS, the growth of the mode with larger spherical harmonic degree (i.e.,  $l \gtrsim 3-4$ ) and thus shorter wavelength tends to be suppressed. As a result, the pattern of the linear unstable mode with lower spherical harmonic degree might be imprinted in the mean flow field like the circulation flow seen in ms100p.

The profile of the differential rotation in ms300p and ms900p is cylindrical (fig.10(c2) & (c3)), that is in the Taylor-Proudman state like as mf60p and mf120p, the flow being constrained to be quasi two-dimensional plane along the spin axis (e.g., Pedlosky 1982; Kitchatinov & Ruediger 1995). The lower the spin rate is, the weaker the rotational constraint on the flow becomes, resulting in the shellular rotation profile seen in ms100p (fig.10(c1)). Such a shellular rotation profile is also observed in Brun & Palacios (2009) for the slowly-rotating red giant. As was described, in relatively-slowly rotating systems, the angular momentum transport is mainly in the radially-inward direction, that is  $\mathcal{F}_{RS} \propto \overline{u'_r u'_\phi} e_r$  with  $\overline{u'_r u'_\phi} < 0$ . The faster spinning motion in the deeper CZ is thus a natural result of the turbulent transport process.

### 3.3.2. Magnetic Field : Dynamo Activities

As shown in Figure 9(b), the spherical-shell convective motion amplifies turbulent magnetic fields of  $\mathcal{O}(10^{16})$  G via small-scale dynamo process (e.g., Cattaneo 1999; Schekochihin et al. 2004). The magnetic energy contained in the turbulent magnetic component is larger with the deeper depths. When taking time and zonal average, we can find, even in *models* ms, that the large-

scale component of the magnetic field is developed in these highly-disordered magnetic fields.

In Figure 12, the meridional distributions of (a)  $\langle\langle B_r \rangle\rangle_\phi$ , (b)  $\langle\langle B_\theta \rangle\rangle_\phi$  and (c)  $\langle\langle B_\phi \rangle\rangle_\phi$  for *models* ms are shown. The top, middle and bottom panels are for *models* ms100p, ms300p, and ms900p, respectively. The time average is taken over the duration  $220 \leq t \leq 240$  ms. The red (blue) tone denotes the positive (negative) magnetic field strength.

As in *models* mf, the mean component of the magnetic field has averagely a strength  $\mathcal{O}(10^{14})$  G and locally exceeds  $10^{15}$  G, which is comparable to the field strength expected in “magnetars”. When focusing on the geometry of the poloidal component of the magnetic field ( $B_r$  and  $B_\theta$ ), we can find it is more complicated than that observed in the models with the full-sphere convection: while the higher multi-pole structure becomes dominant in the models in relatively-slow rotation regime (ms100p and ms300p), the quadrupolar dominance is prominent in the fastest spinning model (ms900p). Additionally to the poloidal component, a large-scale toroidal magnetic component is also built up in all models. Commonly, it is roughly anti-symmetric with respect to the equator and seems to have a strength which is a bit “stronger” than the poloidal magnetic component. The dependence of the large-scale magnetic field on the spin rate and the mechanism for the large-scale dynamo observed in our simulation models are discussed in the following section in detail.

## 4. DISCUSSION

### 4.1. Rotational Dependence of Large-scale Magnetic Field

As presented in Figs. 8 and 12, the mean component of the magnetic field is spontaneously organized in all the PNS models we examined in this paper. Here we discuss the dependence of the structure and strength of the mean magnetic component on the spin rate of the PNS systematically.

To gain quantitative insights into it, the latitudinal moments of the axisymmetric field,  $\bar{\mathbf{B}}$ , is analyzed where the overbar, used to simplify the notation, denotes the time and longitudinal average, i.e.,  $\bar{B}_r = \langle\langle B_r \rangle\rangle_\phi$ . We focus on the radial component  $\bar{B}_r$  since it purely reflects the poloidal field, while  $\bar{B}_\theta$  and  $\bar{B}_\phi$  are a mixture of the toroidal and poloidal fields. From the Perseval’s equation, a relation

$$\langle\langle \bar{B}_r^2 \rangle\rangle_\theta = \frac{1}{2} \sum_{l=1} (\bar{B}_r)_l^2, \quad (17)$$

where

$$(\bar{B}_r)_l = \int_{-1}^1 \bar{B}_r P_l^*(\cos\theta) d\cos\theta, \quad (18)$$

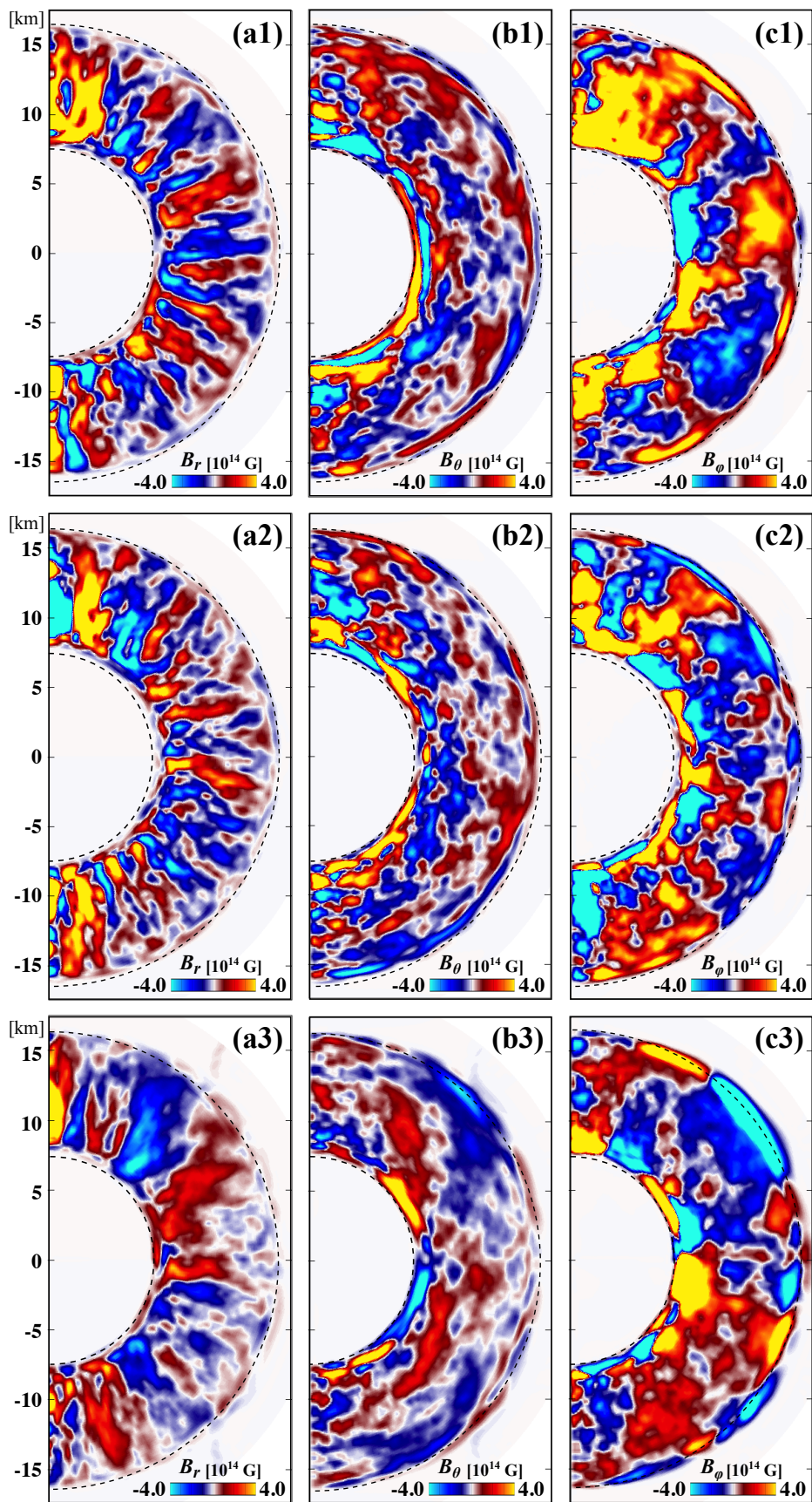


**Figure 12.** Meridional distributions of large-scale magnetic components, (a)  $\langle\langle B_r \rangle\rangle$ , (b)  $\langle\langle B_\theta \rangle\rangle$ , and (c)  $\langle\langle B_\phi \rangle\rangle$  for *model ms*. The top, middle and bottom panels are corresponding to *models* ms100p, ms300p, and ms900p, respectively. The time average is taken over the duration  $220 \leq t \leq 240$  ms.

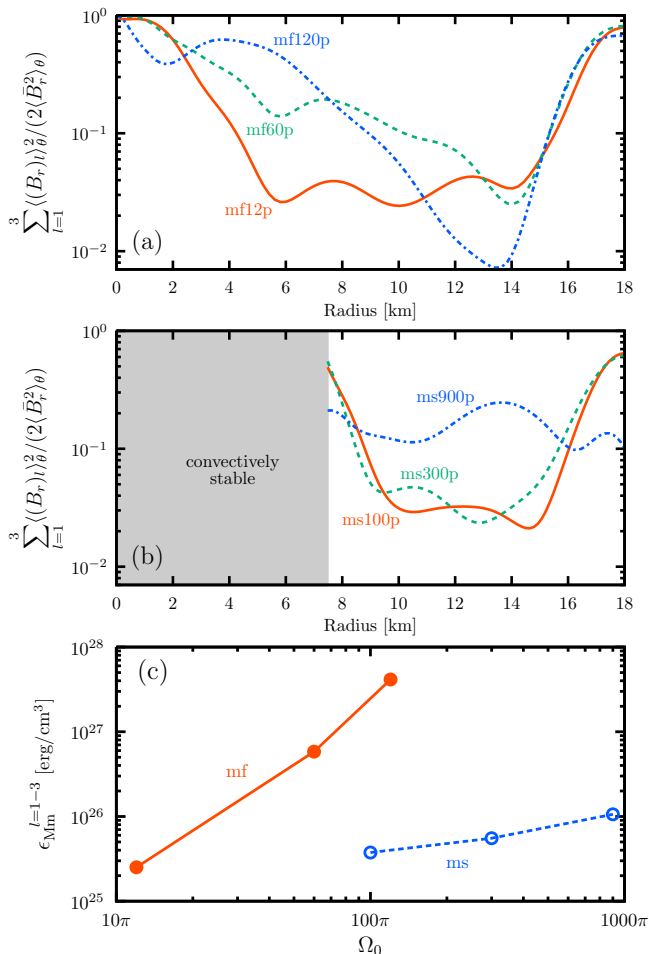


**Figure 13.** Radial distributions of the dominance of the large-scale field for (a) *models* mf and (b) *models* ms. The different line types denote models with different spin rates. Panel (c) shows the dependence of the mean magnetic energy of the large-scale magnetic field on the spin rate for *model* mf (red-solid) and *model* ms (blue-dashed).

holds (see Masada et al. 2013, for details). Here  $P_l^*$  are normalized Legendre polynomials. In the following, we focus on three larger scale modes  $l = 1, 2$ , and  $3$  (dipole, quadrupole, and octapole) as an indicator of the efficiency of the large-scale dynamo.

Shown in Figure 13 is the radial distribution of the ratio of the magnetic energy stored in the largest-scale components ( $l = 1-3$ ) to the total magnetic energy of the axisymmetric field, that is  $\sum_{l=1}^3 \langle (\bar{B}_r)_l \rangle_\theta^2 / (2 \langle \bar{B}_r^2 \rangle_\theta)$  for (a) *models* mf and (b) *models* ms. The different line types denote the models with different spin rates. The gray shaded region in panel (b) corresponds to the convectively-stable region of *models* ms. Note that the higher the ratio, the more the large-scale field becomes dominant.

For *models* mf (panel (a)), the dominance of the large-scale component in the magnetic energy is more pro-

nounced in the deeper CZ and decreases with the radius, suggesting that the dynamo effect is stronger in the deeper depth. Interestingly, even in mf12p with the smallest spin rate (red-solid line), the central part of the PNS ( $r \lesssim 5$  km) is occupied by the large-scale component, which is consistent with the result of Figure 8. As the spin rate increases, the region where the large-scale magnetic component becomes dominant extends into the outer part of the CZ, implying that the dynamo effect becomes stronger in the higher spin rate of the PNS.

Comparing *models* mf and ms, the dominance of the large-scale magnetic component seems to be weaker in the *models* ms. It is a common feature of all the models that the strong large-scale component is developed near the upper and lower boundaries, but in the mid-part of the CZ, only the model ms900p shows a strong large-scale magnetic component (blue dash-dotted line in panel (b)). This implies that the large-scale dynamo can be excited in the mid-part of the CZ only when the PNS's spin is fast enough.

Figure 13(c) shows the dependence, on the spin rate, of the mean magnetic energy stored in the large-scale component defined by

$$\epsilon_{Mm, l=1-3} = \sum_{l=1}^3 \left[ \int_{r_{\min}}^{r_{\max}} (\bar{B}_r)_l^2 dr / \int_{r_{\min}}^{r_{\max}} dr \right], \quad (19)$$

where  $r_{\min}$  and  $r_{\max}$  is the pseudo- upper and lower boundaries of the CZ. We choose  $r_{\min} = 0$  km and  $r_{\max} = 17$  km for *models* mf and  $r_{\min} = 7.5$  km and  $r_{\max} = 17.5$  km for *models* ms.

Commonly in both models, we can find a clear tendency for the mean magnetic energy stored in the large-scale component to increase with the spin rate. However, there exists a difference in the strength of the dependency on the spin rate. In the regime we studied in this paper, the slope of the spin-dependence is steeper in *models* mf than in *models* ms. It would be necessary to investigate the dependence of the PNS dynamo on the spin rate in a wider parameter range to understand the difference in the trends.

#### 4.2. Dynamo Mechanism

It is well known that the rotating convection system spontaneously generates a mean kinetic helicity with a north-south anti-symmetry, i.e., in the case of the eastward spinning motion like our PNS model, bulk negative helicity in north and positive in south, because of the Coriolis force acting on the convection flow (e.g., Miesch 2005; Miesch & Toomre 2009). From preceding studies on stellar and solar dynamos (e.g., Charbonneau 2014; Brun & Browning 2017; Charbonneau 2020, for

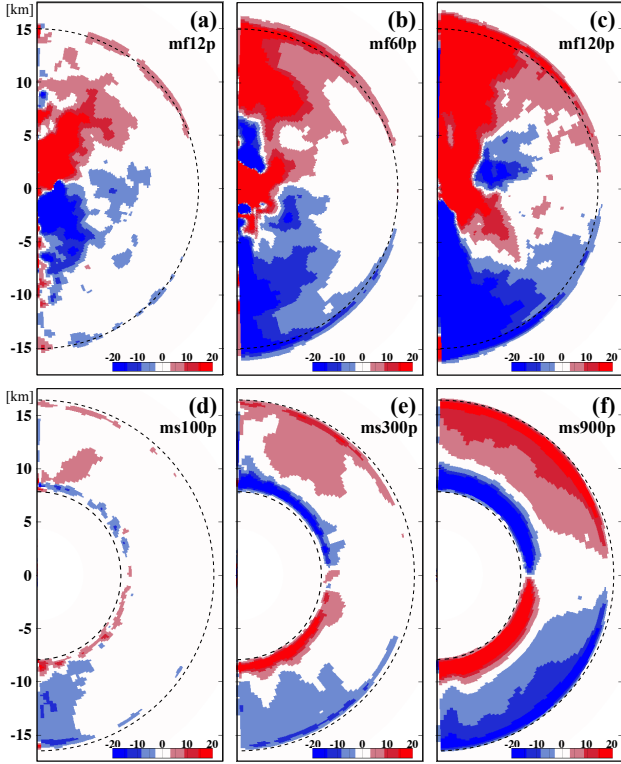


**Figure 14.** Meridional distributions of  $C_\alpha = \alpha H_\rho / \eta_t$  for *models* mf [(a)–(c)] and *models* ms [(d)–(f)].

reviews), we expect that the turbulent electro-motive force (EMF) would be the key for generating the large-scale magnetic component even in our PNS models (e.g., Racine et al. 2011; Masada & Sano 2014).

Although it is difficult to evaluate quantitatively the role of the turbulent EMF in the complicated PNS models, we can appraise it at least qualitatively based on the mean-field dynamo (MFD) theory. Under the first-order smoothing approximation (e.g., Brandenburg & Subramanian 2005; Masada & Sano 2014), the kinetic helicity would be closely linked to the turbulent  $\alpha$ -effect, which is a key ingredient for inducting the large-scale magnetic field in the MFD framework (e.g., Moffatt 1978; Krause & Raedler 1980), as

$$\alpha \equiv -\tau_{\text{cor}} \langle \langle \mathbf{v}' \cdot \boldsymbol{\omega}' \rangle_\phi \rangle / 3, \quad (20)$$

where  $\mathbf{v}' \equiv \mathbf{v} - \langle \langle \mathbf{v} \rangle_\phi \rangle$  is the turbulent velocity,  $\tau_{\text{cor}}$  is the correlation time and  $\boldsymbol{\omega}' \equiv \nabla \times \mathbf{v}'$  is the turbulent vorticity. Additionally to it, the turbulent magnetic diffusivity, which parameterizes the turbulent transport of the magnetic energy through advection and reconnection and thus controls the destruction process of the large-scale magnetic field, is linked to the turbulent velocity as

$$\eta_t \equiv \tau_{\text{cor}} \langle \langle \mathbf{v}'^2 \rangle_\phi \rangle / 3. \quad (21)$$

Essentially, these parameterizations for  $\alpha$  and  $\eta_t$  are valid only in isotropic turbulence (e.g., Schrijver & Siscoe 2010). However, even in an-isotropic turbulence, these have been shown to be useful in studying the ability of a system to excite the large-scale dynamo (e.g., Racine et al. 2011; Masada & Sano 2014).

In eqs.(20) and (21), the correlation time can be evaluated as the convective turn-over time, that is  $\tau_{\text{cor}} = H_\rho / \langle v_r^2 \rangle^{1/2}$ , where  $H_\rho$  is the density scale-height. Since  $\mathbf{v}'$ ,  $\boldsymbol{\omega}'$  and  $H_\rho$  can be extracted from the simulation data directly, we can depict meridional distributions of the turbulent  $\alpha$  and turbulent magnetic diffusivity for each model. In the following, we discuss the hidden connection between the large-scale magnetic component observed in our PNS models and the turbulent EMF with using a non-dimensional parameter  $C_\alpha$  defined by

$$C_\alpha = \alpha H_\rho / \eta_t, \quad (22)$$

which is equivalent to the so-called ‘‘Dynamo number’’ when the  $H_\rho$  is chosen as the typical spatial scale on which the large-scale dynamo works. Since the  $\alpha$  and  $\eta_t$  describes the induction and destruction effects of the large-scale magnetic component respectively, the amplitude of  $C_\alpha$  becomes a measure of the efficiency of the large-scale dynamo.

Shown in Figure 14 is the meridional distribution of  $C_\alpha$  which is derived directly from the simulation data obtained in each model. Panels (a)–(c) correspond to those in *models* mf and panels (d)–(f) are for *models* ms. Note that the color scale is the same for all panels. The darker the color, the stronger the relative induction effect becomes.

Since the kinetic helicity has an anti-symmetric profile with respect to the equator (bulk negative in north and positive in south), the profile of  $C_\alpha$  also shows the quasi-anti-symmetry between hemispheres. With comparing Figs 13 and 14, it can be found that there exists a remarkable overlap between the region with the strong large-scale magnetic component, and the region with the large  $|C_\alpha|$  in both models. In addition to that, the region with the large  $|C_\alpha|$  extends into the outer part of the CZ like as that observed in the large-scale magnetic component. Comparing two models, we can see that the amplitude of  $C_\alpha$  is larger in *models* mf than in *models* ms, suggesting that the higher efficiency of the large-scale dynamo in *models* mf. This is consistent with the stronger large-scale magnetic component in *models* mf seen in Fig.13(c). Overall these results suggest that the turbulent EMF plays an important role in the large-scale dynamo in our PNS models.

Then, a natural question arises ‘‘why is the efficiency of the large-scale dynamo higher in *models* mf though the

spin rate of models *mf* is smaller than that of models *ms* ? ”. The key for it would be the typical size and velocity of the convective motion. The turbulent  $\alpha$ -effect can be brought to the form

$$\alpha = -\frac{1}{3}\tau_{\text{cor}}^2 \mathbf{v}'^2 [\boldsymbol{\Omega} \cdot \nabla \ln(\overline{\rho \mathbf{v}'})] , \quad (23)$$

if we assume that the inhomogeneity arises from the stratification and the symmetry breaking from the Coriolis force, and the lifetime of turbulent eddies is evaluated by the their turnover time (e.g., Charbonneau 2013). With this description, the dynamo number  $\mathcal{C}_\alpha$  can be rewritten as

$$\begin{aligned} \mathcal{C}_\alpha &= \alpha H_\rho / \eta_t \\ &\simeq \Omega H_\rho \cos \theta / v_{\text{rms}} \propto Ro^{-1} , \end{aligned} \quad (24)$$

with a rough estimation,  $\nabla \ln(\overline{\rho \mathbf{v}'}) \simeq 1/H_\rho$ . When ignoring the latitudinal dependence, we can see that the dynamo number, which is a measure of the efficiency of the large-scale dynamo, is a function of the spin rate, the scale-height, and the velocity of the turbulent convective motion.

On the whole, *models mf* are assumed to have lower spin rates than in *models ms*. On the other hand, as shown in figs. 2 and 5, *models mf* has a lower convection velocity and a larger size of the convective eddies especially in the central part of the PNS. These results indicate that the larger  $\mathcal{C}_\alpha$  realized in *models mf* is a consequence of the smaller convection velocity and larger size of the convective eddies (especially in the deeper CZ), which compensate for its smaller spin rate, resulting in the environment more suitable for the large-scale dynamo. It can be said that, physically, the deeper the CZ extends, the larger the size of the convection eddies, and thus the rotationally-constrained convection is more easily achieved, resulting in a region more suitable for the large-scale dynamo.

## 5. SUMMARY

In this paper, we constructed a “PNS in a box” simulation model with solving the compressible MHD with a nuclear EOS and a simplified leptonic transport to study properties of MHD convection and dynamo in PNSs. As a demonstration of our newly-developed model, we applied it to two types of the internal structure of the PNS : fully-convective state and spherical-shell convection state. Our main findings are summarized as follows.

1. The large-scale flows developed in *models mf* are divided into two types : (i) a single-cell meridional circulation with a north-south anti-symmetric differential rotation (mf12p), and (ii) a double-cell meridional circulation (single-cell per hemisphere) with a cylindrical

differential rotation (mf60p and mf120p). While the dipole dominance in  $\delta\epsilon$  is accompanied with the flow pattern (i), the quadrupolar dominance in  $\delta\epsilon$  is developed in conjunction with the pattern (ii).

2. The large-scale flows developed in *models ms* are also divided into two types : (i) multi-cell meridional circulations with a shellular differential rotation (ms100p), and (ii) a double-cell meridional circulation (single-cell per hemisphere) with a cylindrical differential rotation (ms300p and ms900p). While the multipolar structure of  $\delta\epsilon$  is accompanied with the flow pattern (i), the quadrupolar structure of  $\delta\epsilon$  is developed in the models with relatively higher spin rates.

3. With taking account of the angular momentum transport due to the turbulent Reynolds stress caused by rotating convective motions, the circulation pattern of the formed meridional flow can be qualitatively understood by the so-called “gyroscopic pumping”. On the other hand, the profile of the differential rotation is determined to maintain the thermal wind balance of the system.

4. The magnetic field amplified by the PNS convection shows a complicated structure mixed with the turbulent and large-scale components. It should be emphasized that, in all the PNS models we studied here, the large-scale component of the magnetic field is spontaneously organized. For *models mf*, the mean magnetic component exhibits a dipole dominance, i.e., the large-scale poloidal component, rooted deep in the central part of the PNS, shows a strong dipole symmetry. In contrast to that, for *models ms*, while the higher multi-pole structure becomes dominant in the models in a relatively-slow rotation regime, the quadrupolar dominance is prominent in the fastest spinning model.

5. Although there exists a clear tendency for the mean magnetic energy stored in the large-scale component to increase with the spin rate in both models, the slope of the spin-dependence is steeper in *models mf* than in *models ms*. Additionally, it is intriguing that, as an overall trend, *models mf* has a stronger large-scale magnetic component than that in *models ms*.

6. There exists a remarkable overlap between the region with the strong large-scale magnetic component, and the region with the large  $|\mathcal{C}_\alpha|$  in both models, where  $\mathcal{C}_\alpha$  is equivalent to the so-called “dynamo number” and a measure of the efficiency of the large-scale dynamo. Comparing two models, the amplitude of  $\mathcal{C}_\alpha$  is larger in *models mf* than in *models ms*, suggesting that the higher efficiency of the large-scale dynamo in *models mf*. Since the deeper the CZ extends, the larger the size of the convection eddies, the rotationally-constrained convection seems to be more easily achieved in *models mf*. As

a result, the full-sphere convection state becomes more suitable for the large-scale dynamo.

Although the convective dynamo is believed conventionally to work only in rapidly rotating PNSs (e.g., TD93), a clear dynamo activity can be found even in a slowly-rotating PNS with  $P_{\text{rot}} \simeq 200$  ms (mf12p). This would be essentially due to the setup of *models* mf in which the CZ extends to the deeper part of the PNS. It is well-known that the width of the CZ in the PNS changes depending not only on the physical properties of the progenitor star (e.g., Nagakura et al. 2019) but also on the evolution phase of the PNS. As demonstrated in the 2D hydrodynamic simulation of the deleptonization of the PNS by Keil et al. (1996), the CZ in the PNS enlarges to the deeper part with the progress of the neutrino cooling, finally encompassing the whole star within  $\sim 1$  s after bounce, and can continue for at least as long as the deleptonization takes place (see also, Roberts et al. (2012)).

Since most of the existing studies for the PNS dynamo supposes the early evolutionary stage at which only the outer part of the PNS is convective, the scale-height, thus the size of the convective eddies, is relatively small there, resulting in the high  $C_\alpha$  in the case with the slow or moderate rotation (e.g., TD93). On the other hand, at the later evolutionary stage, the PNS is expected to have a deeper CZ with a larger size of the convective eddies in the deeper part like the fully-convective models we studied here. In such a situation, the Coriolis force dominates over the inertia force around the PNS core, and thus the large-scale magnetic component

might be efficiently amplified there by the turbulent  $\alpha$ -effect against the turbulent magnetic diffusion, i.e., the region with  $C_\alpha \gg 1$  might be more easily developed. Overall our results imply that the PNS dynamo may become more efficient in later phases of its evolutionary stage. We note that the importance of the deep core convection for the large-scale dynamo has already been pointed out in the study for the origin of the magnetic field in the fully-convective M-type dwarfs (Yadav et al. 2016; Käpylä 2020). To build up the concrete view on the role of the PNS convection in the context of the origin of NS's magnetic fields, we should study the MHD convection in the PNS in the wider parameter range with varying the depth of the CZ, diffusivities, the rotation rate, and the initial strength of the magnetic field, respectively. These are beyond the scope of this paper, but will be a target of our future work.

This work has been supported by MEXT/JSPS KAKENHI Grant numbers JP17H01130, JP17K14306, JP18H01212, JP18K03700, JP17H06357, JP17H06364, JP18H04444, JP21K03612; the Central Research Institute of Stellar Explosive Phenomena (REISEP) at Fukuoka University and the associated projects (Nos. 171042,177103) and JICFuS as a priority issue to be tackled by using Post 'K' Computer. Numerical computations were carried out on Cray XC50 at Center for Computational Astrophysics, National Astronomical Observatory of Japan.

## REFERENCES

- Bonanno, A., Rezzolla, L., & Urpin, V. 2003, *A&A*, 410, L33
- Bonanno, A., Urpin, V., & Belvedere, G. 2006, *A&A*, 451, 1049
- Brun, A. S. & Toomre, J. 2002, *ApJ*, 570, 865
- Brun, A. S., & Palacios, A. 2009, *ApJ*, 702, 1078
- Brun, A. S., García, R. A., Houdek, G., et al. 2015, *SSRv*, 196, 303
- Brun, A. S., & Browning, M. K. 2017, *Living Reviews in Solar Physics*, 14, 4
- Brandenburg, A., & Subramanian, K. 2005, *PhR*, 417, 1
- Burrows, A., & Lattimer, J. M. 1988, *PhR*, 163, 51
- Camelio, G., Dietrich, T., Marques, M., et al. 2019, *PhRvD*, 100, 123001
- Cattaneo, F. 1999, *ApJL*, 515, L39
- Chandrasekhar, S. 1961, *Hydrodynamic and Hydromagnetic Stability* (Oxford: Clarendon)
- Charbonneau, P. 2013, *Solar and Stellar Dynamos: Saas-Fee Advanced Course 39, Saas-Fee Advanced Courses, Volume 39*. ISBN 978-3-642-32092-7. Springer-Verlag Berlin Heidelberg, 2013, 39. doi:10.1007/978-3-642-32093-4
- Charbonneau, P. 2014, *ARA&A*, 52, 251
- Charbonneau, P. 2020, *Living Reviews in Solar Physics*, 17, 4
- Dobler, W., Stix, M., & Brandenburg, A. 2006, *ApJ*, 638, 336
- Enoto, T., Kisaka, S., & Shibata, S. 2019, *Reports on Progress in Physics*, 82, 106901
- Epstein, R. I. 1979, *MNRAS*, 188, 305
- Fan, Y., & Fang, F. 2014, *ApJ*, 789, 35
- Ferrario, L., Melatos, A., & Zrake, J. 2015, *SSRv*, 191, 77
- Featherstone, N. A. & Miesch, M. S. 2015, *ApJ*, 804, 67

- Freytag, B., Steffen, M., & Dorch, B. 2002, *Astronomische Nachrichten*, 323, 213
- Ghizaru, M., Charbonneau, P., & Smolarkiewicz, P.K. 2010, *ApJL*, 715, L133
- Hobbs, G., Lorimer, D. R., Lyne, A. G., et al. 2005, *MNRAS*, 360, 974
- Hotta, H., Rempel, M., & Yokoyama, T. 2016, *Science*, 351, 1427
- Jones, C. A. 2011, *Annual Review of Fluid Mechanics*, 43, 583
- Käpylä, P.J., Mantere, M.J., & Brandenburg, A. 2012, *ApJL*, 755, L22
- Käpylä, P. J. 2020, arXiv:2012.01259
- Keil, W., Janka, H.-T., & Mueller, E. 1996, *ApJL*, 473, L111
- Kippenhahn, R., & Weigert, A. 1990, *Stellar Structure and Evolution*
- Kitchatinov, L. L. & Ruediger, G. 1995, *A&A*, 299, 446
- Krause, F., & Raedler, K.-H. 1980, *Oxford*
- Lattimer, J. M., & Swesty, D. F. 1991, *NuPhA*, 535, 331
- Ledoux, P. 1947, *ApJ*, 105, 305
- Mabuchi, J., Masada, Y., & Kageyama, A. 2015, *ApJ*, 806, 10
- Masada, Y., Sano, T., & Shibata, K. 2007, *ApJ*, 655, 447
- Masada, Y. 2011, *MNRAS*, 411, L26
- Masada, Y., Takiwaki, T., Kotake, K., et al. 2012, *ApJ*, 759, 110
- Masada, Y., Yamada, K., & Kageyama, A. 2013, *ApJ*, 778, 11
- Masada, Y., & Sano, T. 2014, *ApJL*, 794, L6
- Masada, Y., Takiwaki, T., & Kotake, K. 2015, *ApJL*, 798, L2
- Miesch, M. S. 2005, *Living Reviews in Solar Physics*, 2, 1
- Miesch, M. S., Brun, A. S., & Toomre, J. 2006, *ApJ*, 641, 618
- Miesch, M. S. & Toomre, J. 2009, *Annual Review of Fluid Mechanics*, 41, 317
- Moffatt, H. K. 1978, *Cambridge Monographs on Mechanics and Applied Mathematics*
- Mösta, P., Ott, C. D., Radice, D., et al. 2015, *Nature*, 528, 376
- Nagakura, H., Burrows, A., Radice, D., et al. 2019, arXiv:1912.07615
- Nordlund, Å., Galsgaard, K., & Stein, R. F. 1994, *NATO Advanced Science Institutes (ASI) Series C*, 471
- Ott, C. D., Burrows, A., Thompson, T. A., et al. 2006, *ApJS*, 164, 130
- Parker, E. N. 1955, *ApJ*, 122, 293
- Pedlosky, J. 1982, *Geophysical Fluid Dynamics* (Springer)
- Pons, J. A., Reddy, S., Prakash, M., et al. 1999, *ApJ*, 513, 780
- Rheinhardt, M. & Geppert, U. 2005, *A&A*, 435, 201.
- Racine, É., Charbonneau, P., Ghizaru, M., et al. 2011, *ApJ*, 735, 46
- Raynaud R., Guilet J., Janka T. and Gastine, T, *Science Advances*,
- Roberts, L. F., Shen, G., Cirigliano, V., et al. 2012, *PhRvL*, 108, 061103
- Ruderman, M. 1972, *ARA&A*, 10, 427
- Ruderman, M. A., & Sutherland, P. G. 1973, *Nature Physical Science*, 246, 93
- Sano, T., Inutsuka, S., & Miyama, S. M. 1999, *Numerical Astrophysics*, 383
- Scheck, L., Kifonidis, K., Janka, H.-T., et al. 2006, *A&A*, 457, 963.
- Schrijver, C. J. & Siscoe, G. L. 2010, *Heliophysics: Evolving Solar Activity and the Climates of Space and Earth*, Edited by Carolus J. Schrijver and George L. Siscoe. Published by Cambridge University Press, London 2010.
- Schekochihin, A. A., Cowley, S. C., Taylor, S. F., et al. 2004, *ApJ*, 612, 276
- Spruit, H. C. 2008, *40 Years of Pulsars: Millisecond Pulsars, Magnetars and More*, 391
- Tassoul, J.-L. 2000, *Stellar rotation / Jean-Louis Tassoul*. Cambridge University Press
- Torres-Forné, A., Cerdá-Durán, P., Passamonti, A., et al. 2019, *MNRAS*, 482, 3967. doi:10.1093/mnras/sty2854
- Turolla, R., Zane, S., & Watts, A. L. 2015, *Reports on Progress in Physics*, 78, 116901
- Thompson, C., & Duncan, R. C. 1993, *ApJ*, 408, 194
- Yadav, R. K., Christensen, U. R., Wolk, S. J., et al. 2016, *ApJL*, 833, L28